APSB
Acta Pharmaceutica Sinica B

2022
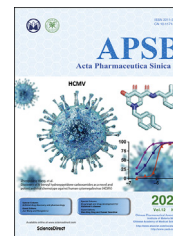
ORIGINAL ARTICLE

Remodeling "cold" tumor immune microenvironment *via* epigenetic-based therapy using targeted liposomes with *in situ* formed albumin corona

Yang He[a,b,c,d,†], Yuefei Fang[a,e,†], Meng Zhang[a,f], Yuge Zhao[a], Bin Tu[a,b], Mingjie Shi[a], Bahtiyor Muhitdinov[a,g], Akmal Asrorov[a,g], Qin Xu[e], Yongzhuo Huang[a,b,c,h,*]

[a]*State Key Laboratory of Drug Research, Shanghai Institute of Materia Medica, Chinese Academy of Sciences, Shanghai 201203, China*
[b]*University of Chinese Academy of Sciences, Beijing 100049, China*
[c]*Zhongshan Institute for Drug Discovery, Chinese Academy of Sciences, Zhongshan 528437, China*
[d]*Department of Pharmacy, the First Affiliated Hospital of Zhengzhou University, Zhengzhou 450052, China*
[e]*Artemisinin Research Center, Guangzhou University of Chinese Medicine, Guangzhou 510450, China*
[f]*Women's Hospital, School of Medicine, Zhejiang University, Hangzhou 310006, China*
[g]*Institute of Bioorganic Chemistry, Uzbekistan Academy of Sciences, Tashkent 100125, Uzbekistan*
[h]*National Medical Products Administration, Key Laboratory for Quality Research and Evaluation of Pharmaceutical Excipients, Shanghai 201203, China*

Abstract   There is a close connection between epigenetic regulation, cancer metabolism, and immunology. The combination of epigenetic therapy and immunotherapy provides a promising avenue for cancer management. As an epigenetic regulator of histone acetylation, panobinostat can induce histone acetylation and inhibit tumor cell proliferation, as well as regulate aerobic glycolysis and reprogram intratumoral immune cells. JQ1 is a BRD4 inhibitor that can suppress PD-L1 expression. Herein, we proposed a chemo-free, epigenetic-based combination therapy of panobinostat/JQ1 for metastatic colorectal cancer. A novel targeted binary-drug liposome was developed based on lactoferrin-mediated binding with the LRP-1 receptor. It was found that the tumor-targeted delivery was further enhanced by *in situ*

*Corresponding author. Tel./fax: +86 2120231981.

E-mail address: yzhuang@simm.ac.cn (Yongzhuo Huang).

[†]These authors made equal contributions to this work.

formation of albumin corona. The lactoferrin modification and endogenous albumin adsorption contribute a dual-targeting effect on the receptors of both LRP-1 and SPARC that were overexpressed in tumor cells and immune cells (*e.g.*, tumor-associated macrophages). The targeted liposomal therapy was effective to suppress the crosstalk between tumor metabolism and immune evasion *via* glycolysis inhibition and immune normalization. Consequently, lactic acid production was reduced and angiogenesis inhibited; TAM switched to an anti-tumor phenotype, and the anti-tumor function of the effector $CD8^+$ T cells was reinforced. The strategy provides a potential method for remodeling the tumor immune microenvironment (TIME).

1. Introduction

Colorectal cancer (CRC) is the third most common cancer, and metastasis is the main cause that contributes to CRC-associated death[1]. Notably, the 5-year survival rate of CRC patients is less than 10%[2]. Although several molecularly targeted drugs (*e.g.*, EGFR mAbs and BRAF tyrosine kinase inhibitors) have been studied in clinical trials, the regimen of a single-target drug shows little benefit to CRC patients[3]. Generally, CRC can be considered as a "cold" tumor and the majority of CRC patients are poorly immune responsive; merely 15% of CRCs are dMMR−MSI-H (mismatch-repair-deficient and microsatellite instability-high), which is a positive prognosis biomarker for immunotherapy[4].

The occurrence and development of cancers are the results of genetic mutations and epigenetic changes. The structural changes of transcription factors and DNA-binding proteins can regulate the expression of the oncogene[5]. For instance, histone deacetylase inhibitors (HDACi) are a class of histone epigenetic modification regulators that make histone H3 and H4 highly acetylated by inhibiting the activity of histone deacetylase, and acetylation promotes the depolymerization of chromatin and the consequent inhibition of transcription of the oncogenes and DNA repair genes[6].

HDACi have been clinically used as an effective treatment for blood cancer[7], which can induce tumor cell apoptosis, cell cycle arrest, autophagy, and anti-angiogenesis[8]. However, there is very limited clinical success in solid tumors with HDACi; combination therapy is considered to be a potential solution to this issue[9]. Apart from restoring acetylation homeostasis in cancer cells, HDACi can also trigger tumor immunity; for example, they can "re-educate" the M2-like tumor-associated macrophages (TAM) to the anti-tumor M1 phenotype[10], promote dendritic cell (DC) maturation[11], activate the effector cells such as NK and T cells, and inhibit Treg cells[5,6]. Moreover, HDACi can regulate tumor metabolism by inhibiting the key enzymes or transporters of aerobic glycolysis[12]. Panobinostat (Pano) is an HDACi approved by the US Food and Drug Administration (FDA) in 2015. Pano can activate antigen-specific T cells[13], but the effect on regulating TAM and tumor immune microenvironment (TIME) is barely explored.

Bromodomain and extraterminal (BET) proteins (*e.g.*, BRD4) are epigenetic readers for regulating gene transcription. As a case in point, BRD4 occupies the PD-L1 transcriptional start site and controls PD-L1 expression, and thereby BRD4 inhibitors (*e.g.*, JQ1) have been often explored in PD-1/PD-L1 immune checkpoint blockade (ICB) treatment[14,15]. For example, combining BRD4 inhibitors and ICB drugs can activate T cells and induce durable anti-tumor responses in lung adenocarcinoma[16]. We previously demonstrated that JQ1 cooperated with irinotecan to elicit antitumor immunity in colorectal cancer through inducing immune cell death and suppressing the PD-1/PD-L1 pathway[17].

Epigenetic regulation can enhance the effectiveness of ICB treatment, and epigenetic therapy for anticancer immunity represents a potential avenue[18]. In this work, we thus proposed an epigenetics-based, chemo-free combination therapy using a liposomal targeting codelivery of Pano/JQ1 to improve treatment efficacy in colon cancer *via* epigenetic regulation. It was expected that the combination of HDAC and BRD4 inhibitors could simultaneously repolarize TAM and induce ICB, thus remodeling TIME.

A biomimetic targeted delivery strategy was developed by using lactoferrin (LF) to modify the liposomal co-delivery system to treat an immune-inactive CT26 colorectal tumor, which is characterized by its microsatellite stability (MSS) and poor response to PD-1/PD-L1 immunotherapy[19,20]. LF is often used as a targeting ligand in cancer nanomedicine[21]. Both CT26 cancer cells and TAM highly express low-density lipoprotein receptor-associated protein 1 (LRP-1) that possesses a high binding affinity to LF[22]. Therefore, LF-mediated delivery provides a unique benefit of simultaneously targeting cancer cells and TAM, thus facilitating the action of remodeling TIME by reprograming the immunosuppressive cells[23].

Notably, *in vivo* formation of protein corona could influence the biofate of nanomedicine[24]. In this work, the *in situ* formed albumin corona was investigated for the synergistic effect on mediating tumor delivery.

2. Materials and methods

2.1. Materials

Panobinostat and JQ1 (CSNpharm, Chicago, IL, USA). Egg yolk lecithin (PC-98T), soy lecithin, cholesterol, DSPE-PEG$_{2000}$, and DSPE-PEG$_{2000}$-NHS (Advanced Vehicle Technology Co., Ltd., Shanghai, China). Lactoferrin (Nanjing Shengsai Chemical Co., Ltd., Nanjing, China). Bovine serum albumin (BSA) (Amresco, Houston, TX, USA). D-Luciferin potassium salt (PerkinElmer, Waltham, MA, USA). The apoptosis kit, 5-FITC, DiD, and DiR iodide (Meilun Biotechnology, Dalian, China). γH2AX (ABclonal Technology, Wuhan, China). Glyceraldehyde-3-phosphate dehydrogenase (GAPDH), antibodies of Tubulin, BRD4, HIF-1α, C-MYC, HDAC2, CD31, BCL-XL, caspase3, p-STAT6, and iNOS (PE conjugate) (Cell Signaling Technology, Boston, MA, USA). Anti-β-Actin (Sigma−Aldrich, St. Louis, MI, USA). Anti-VEGF

(R&D Systems, Minneapolis, MN, USA). Antibodies of mannose receptor (CD206), PKM2, PD-L1, LRP-1, VEGFR2, Gr-1, and TGF-β1 (Abcam, Cambridge, UK). The anti-SPARC antibody and anti-iNOS antibody (Absin, Shanghai, China). The horseradish peroxidase (HRP)-conjugated goat anti-rabbit/mouse, donkey anti-goat IgG secondary antibody, and Alexa Fluor® 488 Affini-Pure goat anti-rabbit IgG (H + L) (Beyotime, Shanghai, China). Hyaluronidase and collagenase (YEASEN, Shanghai, China). Murine M-CSF, IL-4, and IFN-γ (Peprotech, Rocky Hill, NJ, USA). Lipopolysaccharide (LPS) (Sigma−Aldrich, St. Louis, MI, USA). Purified rat anti-mouse CD16/CD32 (mouse BD Fc block), FITC rat anti-mouse CD49b, APC rat anti-mouse NK1.1, PE rat anti-mouse Ly6G-Ly6C, BB700 rat anti-mouse CD11b, PerCP hamster anti-mouse CD3ε, APC rat anti-mouse CD8α, APC rat anti-mouse PD-L1, PE rat anti-mouse TGF-β, and APC-Cy7 rat anti-mouse IFN-γ (BD Pharmingen, Franklin Lakes, NJ, USA). FITC rat anti-mouse CD45, FITC rat anti-mouse F4/80, APC rat anti-mouse CD206, and PE-Cy7 rat anti-mouse CD206 (Biolegend, San Diego, CA, USA). PE anti-mouse granzyme B (Invitrogen, Carlsbad, CA, USA). InVivoMab anti-mouse PD-1 (BioXcell, Lebanon, NH, USA). Mouse lymphocyte separation medium (Dakewe Biotech Co., Ltd., Shenzhen, China). All other reagents were of analytical grade (Sinopharm Chemical Reagent Co., Ltd., Shanghai, China).

2.2. Cell lines

The murine colorectal cancer cell (CT26) and human umbilical vein endothelial cell (HUVEC) were obtained from the Shanghai Cell Bank of Chinese Academy of Sciences (Shanghai, China). CT26 and CT26-Luc were cultured in RPMI-1640 medium with 10% FBS (Gemini Bio, West Sacramento, CA, USA) and 1% penicillin-streptomycin (Beyotime, Shanghai, China). HUVEC was cultured in Dulbecco's modified Eagle media (DMEM) with 10% FBS and 1% penicillin-streptomycin. All cells were maintained at a humidified 5% CO_2 incubator at 37 °C.

2.3. Animals

Female BALB/c mice (18−22 g) (Shanghai Laboratory Animal Center Co., Ltd., Shanghai, China), were housed at the specific pathogen-free (SPF) care facility. All experimental procedures were executed according to the protocols approved by the Institutional Animal Care and Use Committee (IACUC), Shanghai Institute of Materia Medica (SIMM), Chinese Academy of Sciences, China.

2.4. Collection and polarization of bone marrow-derived macrophage (BMDM, MΦ)

The BALB/c mice were humanely sacrificed and the BMDMs were obtained by using a standard protocol as described in a previous report[10]. The cells were cultured in DMEM with 20% FBS, 1% penicillin-streptomycin, and 20 ng/mL M-CSF at 37 °C for three days. The BMDMs were induced for M1 polarization with 100 ng/mL LPS and 20 ng/mL IFN-γ, or for M2 polarization with 40 ng/mL IL-4.

2.5. In vitro cell viability assay

The CT26 cells or BMDMs were seeded in a 96-well plate at a density of 5×10^3 cells/well. After incubation at 37 °C for 24 h,

the cells were treated with free Pano, free JQ1, combined Pano and JQ1 (termed as Pano + JQ1), Lipo, or LF-Lipo, respectively, for 24 or 48 h. Then a standard MTT method was conducted to measure cell viability. The synergy of Pano and JQ1 was evaluated by calculating the combination index (CI).

2.6. Lactic acid secretion assay

The concentration of lactic acid in the CT26 cell culture medium or the tumor tissues was detected by a lactic acid assay kit (Jiancheng Bioengineering Co., Ltd., Nanjing, China).

2.7. Co-culture system of CT26 tumor cells and MΦ

The co-culture system was utilized to mimic the physiological or pathological conditions. In the study of the effect of CT26 on MΦ, MΦ were seeded in a 12-well transwell plate at a density of 1×10^5 cells/well, while the CT26 tumor cells were seeded in an upper chamber with a polyester membrane (0.4 μm pore, Corning, Corning, NY, USA) at the same density. After incubation for a specified time, both cells were treated with an equivalent drug dose. In the study of the effect of MΦ on CT26 tumor cells, the MΦ were seeded in the upper while the CT26 cells in the lower chambers and other conditions remained the same.

2.8. In vitro M2Φ re-education study

For a mono-culture system, MΦ were seeded in a 12-well plate at a density of 1×10^5 cells/well and cultured for 24 h. The cells were treated with Pano (0.2 μmol/L), JQ1 (0.4 μmol/L), or Pano (0.2 μmol/L) + JQ1 (0.4 μmol/L), respectively, for 24 h.

For a co-culture system, MΦ were seeded in a lower chamber and CT26 cells were seeded in an upper chamber. After 12 h incubation, both cells were treated with Pano (0.2 μmol/L), JQ1 (0.4 μmol/L), or Pano (0.2 μmol/L) + JQ1 (0.4 μmol/L), respectively, for 24 h. After treatment, the MΦ were collected and then subjected to a standard Western blot assay or a standard flow cytometry analysis.

2.9. Preparation of LF-Lipo

In order to evaluate the feasibility of chemical conjugation between LF and DSPE-PEG-NHS, the amidation reaction was examined (Supporting Information Fig. S1). Briefly, 10 mg LF and 1 mg DSPE-PEG-NHS were dissolved in phosphate buffer saline (PBS). The reaction system was incubated at 4 °C for 12 h. Small molecule compounds in the system were removed by dialysis (MWCO 14,000 Da). The LF and DSPE-PEG-LF were freeze-dried and characterized by MALDI-TOF, ^{1}H NMR, and ^{13}C NMR.

The binary-drug LF-modified liposomes (termed LF-Lipo) were prepared by a thin-film dispersion method. Lecithin, cholesterol, DSPE-PEG$_{2000}$, DSPE-PEG-NHS, panobinostat, and JQ1 were dissolved at a mass ratio of 30:1:1:1:1:2 in 9 mL dichloromethane/methanol (2:1, v/v), and the mass of lecithin was 30 mg. The organic solvents were removed by rotary evaporation under vacuum until the thin film of lipid was formed. The thin film was hydrated by 1 mL PBS to form an aqueous suspension, which was then extruded through 0.4 and 0.2 μm polycarbonate membranes with an extruder (Avanti Polar Lipids, Alabaster, AL, USA). 10 mg LF (LF/DSPE-PEG-NHS, 10:1, w/w) was added into the liposome suspension for incubation at 4 °C for 12 h, thus forming the LF-Lip. The unreacted LF was removed by 4500 rpm

centrifugation (ThermoFisher Scientific, Waltham, MA, USA) for 1 h using an Amico filter device (100 K). Non-modified liposome was prepared in the same manner (termed as Lipo). Both the Lipo and LF-Lipo were purified by a Sephadex G-50 column (GE Healthcare, Boston, MA, USA) to get rid of unencapsulated drugs.

2.10. Characterization of LF-Lipo

The modification efficiency of LF on LF-Lipo was determined by SDS-PAGE and quantitatively analyzed by ImageJ software (National Institutes of Health, Bethesda, MD, USA). The particle size, polydisperse index (PDI), and zeta potential of Lipo and LF-Lipo were measured by a Zeta Sizer Nanoparticle Analyzer (Malvern Panalytical, Malvern, UK). The morphological observation of the liposomes was performed using transmission electron microscopy (TEM). The drug encapsulation efficiency (EE%) and drug-loading capacity (DL%) of the liposomes were determined by high-performance liquid chromatography (HPLC) (1260 Infinity, Agilent technologies, Santa Clara, CA, USA) equipped with Diamonsil-C18 (5 μm, 250 mm × 4.6 mm, Dikma, Beijing, China). The chromatographic conditions are listed in Supporting Information Tables S1 and S2.

2.11. Stability and in vitro release

The stability was detected by suspending the liposomes in PBS containing 10% FBS and shaking the suspension (150 rpm) at 37 °C. Particle size change of the liposomes was measured by a Zeta Sizer Nanoparticle Analyzer at a specified time interval. The in vitro drug release was performed by placing liposomes in dialysis bags (MWCO 14,000 Da) in PBS (pH 7.4) containing 1% (w/v) SDS with gently shaking (150 rpm) at 37 °C. A portion of the release medium (1 mL) was sampled for HPLC analysis and an equivalent volume of fresh medium was replenished at the preset time course.

2.12. Cellular uptake assay

The CT26 cells were seeded in a 12-well plate at a density of 1×10^5 cells/well and cultured for 24 h. The cells were treated with equivalent 5-FITC dye-encapsulated Lipo or LF-Lipo (5-FITC/lecithin, 1 mg/30 mg) for 2 h under 37 °C. Afterward, the cells were washed with PBS three times, fixed in 4% paraformaldehyde (PFA) for 20 min, and stained with DAPI. Fluorescent images were obtained by the inverted fluorescence microscope (CARL ZEISS, Oberkochen, Germany).

Besides, the CT26 cells or BMDMs were seeded in a 12-well plate at a density of 1×10^5 cells/well and cultured for 24 h, respectively. The cells were then treated with equivalent 5-FITC dye-encapsulated Lipo or LF-Lipo (5-FITC/lecithin, 1 mg/30 mg) for 2 h incubation at 37 °C. The cells were washed with PBS three times and collected. The quantitative cellular uptake efficiency was detected by a standard flow cytometry analysis.

2.13. Penetration of tumor spheroid

The 60 μL 1% (w/v) agarose gel was pre-covered in the 96-well plates. The CT26 cells were seeded at a density of 5×10^3 cells/well and cultured at 37 °C for 7 days. When the cell cluster formed tumor spheroids, they were treated with equivalent Cy5 dye-encapsulated Lipo or LF-Lipo (Cy5/lecithin, 0.25 mg/30 mg) for 6 h. The tumor spheroids were collected and rinsed by

PBS three times, and then subjected to confocal laser scanning microscope (CLSM) Z-stack (TCS-SP8, Leica, Wetzlar, Germany).

Besides, to investigate the permeability-promoting ability of protein corona, the tumor spheroids were preincubated with serum-free cell culture medium for 12 h and then were treated with equivalent DiD dye-encapsulated LF-Lipo (DiD/lecithin, 0.25 mg/30 mg) or the FBS-containing medium-preincubated LF-Lipo for 4 h. The tumor spheroids were collected and rinsed by PBS three times, and then subjected to CLSM (Leica).

2.14. Characterization of BSA protein corona

The 100 μL liposomes were incubated with the FBS-containing culture medium (1:4, v/v) or plasma (1:1, v/v) for 1 h under 37 °C. The suspension was then diluted with PBS and centrifuged using an Amico filter device (100 K) to remove free proteins. The pellet was rinsed with PBS twice. The adsorption efficiency of albumin on liposomes was determined by a standard SDS-PAGE assay and quantitatively analyzed by ImageJ software. An equivalent cell culture medium aliquot without centrifugation was set as the control.

2.15. Preparation of empty BSA NP

The empty BSA NP was prepared through a homogenization-evaporation method. Briefly, 50 mg soy lecithin was dissolved in 1 mL oil phase (alcohol/chloroform = 2:1, v/v) and 50 mg BSA was dissolved in 4 mL aqueous phase. The primary emulsion was obtained by adding the oil phase to the aqueous phase dropwise under the ultrasonic process. Subsequently, the primary emulsion was subjected to a high-pressure homogenizer (EmulsiFlex-B15, Avestin Inc., Ottawa, Canada) for 10 cycles of homogenization. Alcohol and chloroform were then removed by rotary evaporation. The BSA NP was collected by centrifugation and free BSA was removed.

2.16. Cell apoptosis assay

The CT26 tumor cells were seeded in a 12-well plate at a density of 1×10^5 cells/well and cultured for 24 h. The cells were treated with Pano (0.1 μmol/L), JQ1 (0.2 μmol/L), Pano (0.1 μmol/L) + JQ1 (0.2 μmol/L), Lipo, or LF-Lipo respectively, for 24 h. The cells were then collected and subjected to a standard Western blot assay or a standard flow cytometry analysis using Annexin V-FITC/PI staining.

2.17. Anti-angiogenesis assay

The HUVECs were seeded in a 24-well Transwell plate at a density of 2×10^5 cells/well pretreated with 100 μL matrigel matrix (Corning), and M1Φ (or M2Φ) were seeded in an upper chamber. Both the lower and upper chambers were treated with equivalent Pano (1 μmol/L), JQ1 (2 μmol/L), Pano (1 μmol/L) + JQ1 (2 μmol/L), Lipo, or LF-Lipo respectively, for 12 h. The endothelial cell tube formation was observed by the inverted microscope (ZEISS) in a bright field (10×).

Besides, the HUVECs were seeded in a lower chamber of a Transwell plate, and M1Φ (or M2Φ) were seeded in an upper chamber. Both the lower and upper chamber were treated with the same drugs as mentioned above for 12 h. The HUVECs were then washed, collected, and treated with RIPA lysate (Beyotime,

Shanghai, China). The expression level of VEGFR2 and C-MYC was detected by a standard Western blot analysis.

2.18. Establishment of the CT26 subcutaneous and peritoneal tumor animal models

The CT26 subcutaneous tumor animal models were established by s.c. injection of the CT26 cells (3×10^5) into the back of BALB/c female mice. The CT26 peritoneal metastasis animal models were established by i.p. injection of CT26-Luc cells (3×10^5) into the peritoneum of the BALB/c female mice. The development of CT26 peritoneal tumors was monitored by bioluminescence imaging of IVIS (Caliper PerkinElmer, Waltham, MA, USA) after intravenous injection of D-Luciferin potassium salt (150 mg/kg).

2.19. In vivo imaging and biodistribution

For both CT26 subcutaneous and peritoneal tumor animal models, the BALB/c tumor-bearing mice ($n = 3$) were given the equivalent DiR dye-encapsulated Lipo or LF-Lipo via tail vein injection (1.5 mg/kg). The in vivo imaging study was monitored using IVIS at the pre-set time points. After 24 h, the mice were humanely sacrificed and the tumors and major organs were collected for ex vivo imaging.

For the colocalization study, the isolated tumors were fixed with 4% PFA for 48 h and then dehydrated in 30% sucrose solution for the preparation of cryosection (CM1950, Leica, Weztlar, Germany). The cryosection slides were incubated with the anti-LRP-1 antibody at 4 °C overnight and subsequently labeled by an Alexa Fluor® 488-conjugated secondary antibody and DAPI. The slides were observed by CLSM.

Furthermore, for the quantitative assay of colocalization, the CT26 subcutaneous tumor-bearing mice ($n = 3$) were intravenously injected with equivalent DiD dye-encapsulated Lipo or LF-Lipo (1.5 mg/kg). At 24 h, the mice were humanely sacrificed, and the tumors were collected and digested into individual single cells with hyaluronidase and collagenase. These cells were then stained with anti-LRP-1 antibody followed by Alexa Fluor® 488 fluorescent antibody labeling. The quantitative analysis was conducted using flow cytometry.

2.20. In vivo anti-tumor therapy

For the CT26 subcutaneous tumor animal model, the tumor-bearing mice were randomly divided into six groups (six mice per group). On Day 6 post-inoculation, the mice were treated with PBS (control), Pano (5 mg/kg), JQ1 (10 mg/kg), Pano + JQ1 (Pano 5 mg/kg, JQ1 10 mg/kg), Lipo, or LF-Lipo (equal dose to the combo free drugs), respectively, via tail vein injection every two days. The tumor volume was calculated using the following Eq. (1):

$$\text{Tumor volume (mm}^3) = \text{Length} \times \text{Width}^2/2 \qquad (1)$$

At the endpoint of the therapy, the mice were humanely sacrificed and the tumors and major organs were collected for further study.

For the CT26 peritoneal metastasis animal model, the tumor-bearing mice were randomly divided into six groups (five mice per group). On Day 4 post-inoculation, the mice were treated as described above. At the endpoint, the mice were humanely sacrificed and the tumors were collected for further study.

For the CT26 subcutaneous tumor in situ recurrence model, the tumor-bearing mice were randomly divided into five groups (five mice per group). On Day 8 post-inoculation, the mice were treated with PBS (control), αPD-1 (10 mg/kg), Pano + JQ1 (Pano 5 mg/kg, JQ1 10 mg/kg), LF-Lipo (equal dose to the combo free drugs), and LF-Lipo + αPD-1, respectively, via tail vein injection except for αPD-1 (i.p. injection) every two days. At the therapeutic endpoint, the tumors were surgically removed from the mice. The in situ tumor recurrence was monitored to evaluate the treatment efficacy and immune memory.

2.21. Statistical methods

Data were shown as mean ± standard deviation (SD, $n \geq 3$). The statistical analysis was performed by the t-test and one-way ANOVA. Statistically, the significant difference was defined as *$P < 0.05$, **$P < 0.01$, ***$P < 0.001$, and ****$P < 0.0001$, ns means not significant.

3. Results

3.1. Synergistic anti-tumor effect of Pano/JQ1

The anti-proliferative activity of Pano and JQ1 in CT26 cells was examined. Both the single drugs showed little cytotoxicity, but the synergistic effect was remarkable (Fig. 1A). The combination index (CI) revealed that the optimal ratio of Pano/JQ1 was 1:2 (Supporting Information Table S3), and this ratio was used for the following studies. Both Pano and JQ1 are epigenetic drugs and they can regulate the oncogene expression in an epigenetic way. In addition, it was found that Pano/JQ1 could synergistically inhibit the DNA damage repair process that is an essential survival mechanism for the cancer cells, as shown by the upregulated γH2AX (Fig. 1B), a biomarker of DNA damage, after drug treatment. Therefore, the synergistic cytotoxicity of Pano/JQ1 might be attributed to the elevated DNA damage level.
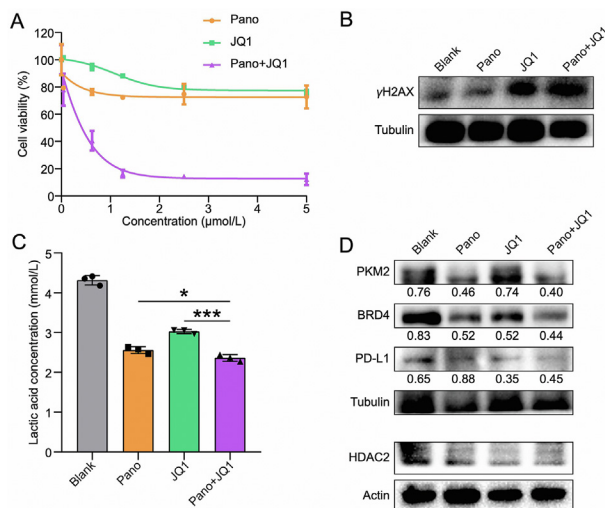

Figure 1 Anticancer effect of Pano and JQ1 in CT26 cells. (A) Cytotoxicity test in CT26 cells. (B) Expression of γH2AX in CT26 cells after treatment. (C) The reduced lactic acid production in CT26 cells after treatment. (D) Expression of PKM2, BRD4, PD-L1, and HDAC2 in CT26 cells after treatment. Data are presented as mean ± SD ($n = 3$). *$P < 0.05$, ***$P < 0.001$.

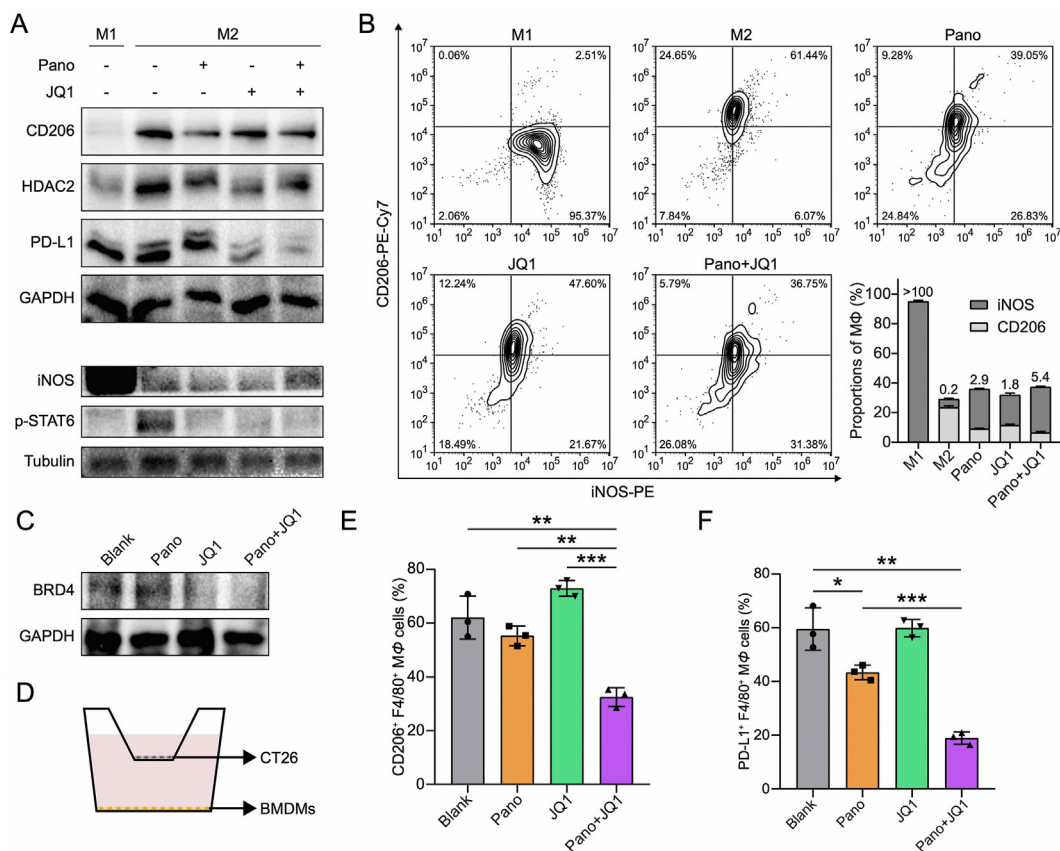**Figure 2** Macrophage regulation of Pano and JQ1. (A) Expression of CD206, HDAC2, PD-L1, iNOS, and p-STAT6 in M1Φ/M2Φ after treatment. (B) MΦ repolarization by Pano and JQ1 treatment. (C) Reduced BRD4 expression in M2Φ after treatment. (D) Illustration of the co-culture system of BMDMs and CT26 cells. (E) Statistical analysis of CD206$^+$ F4/80$^+$ MΦ after treatment. (F) Statistical analysis of PD-L1$^+$ F4/80$^+$ MΦ after treatment. Data are presented as mean ± SD ($n = 3$). *$P < 0.05$, **$P < 0.01$, ***$P < 0.001$.
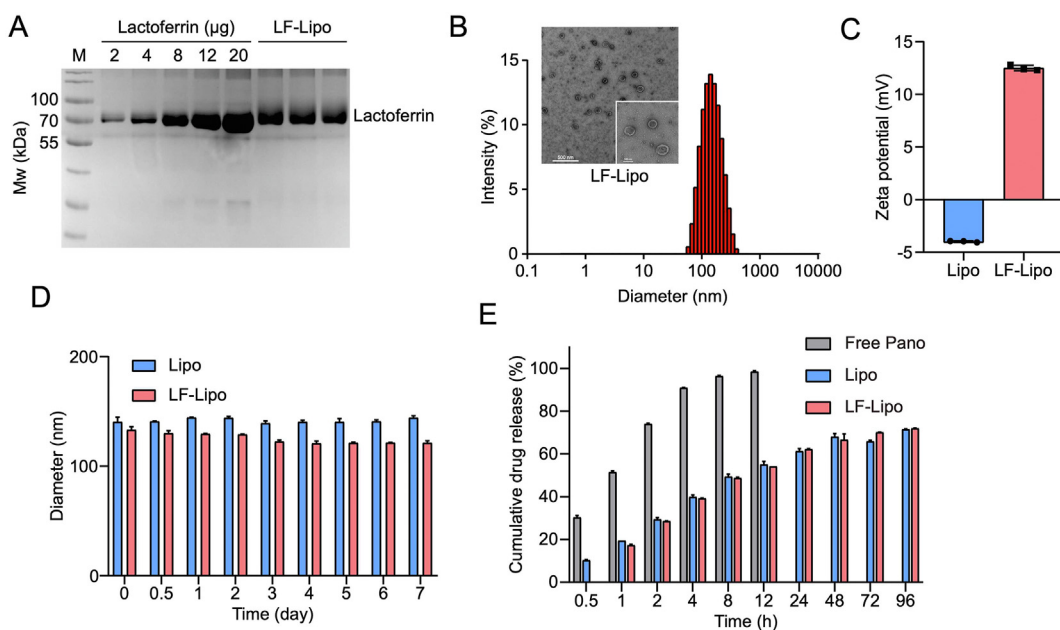

Figure 3 Characterization of the codelivery liposomes. (A) The modification ratio of lactoferrin in LF-Lipo (M, marker). (B) Particle size distribution and TEM image of LF-Lipo. (C) Zeta potential of Lipo and LF-Lipo. (D) Stability of Lipo and LF-Lipo in PBS containing 10% FBS. (E) Cumulative release of Pano in Lipo and LF-Lipo. Data are presented as mean ± SD ($n = 3$).

Histone deacetylation favors transcriptional repression of gluconeogenic enzymes and consequent activation of the glycolytic pathway in cancer cells, leading to the Warburg effect[25]. Therefore, HDAC inhibition serves as a promising therapeutic method to suppress aerobic glycolysis in tumors[26]. The lactic acid in TME is a product of aerobic glycolysis. Our results indicated that the combination of Pano and JQ1 showed a lower level of lactic acid in the CT26 cells compared with a single drug (Fig. 1C). The intrinsic mechanism could be associated with the inhibition of pyruvate kinase M2 (PKM2, Fig. 1D), which is a key metabolic enzyme in aerobic glycolysis. Meanwhile, HDAC2 was downregulated in CT26 cells after treatment (Fig. 1D).

JQ1 is a BRD4 inhibitor. By inhibiting BRD4, JQ1 can decrease BRD4 occupancy at the PD-L1 locus, resulting in the transcriptional pausing and rapid loss of PD-L1 mRNA production, and therefore, JQ1 can suppress PD-L1 expression *via* BRD4-PD-L1 axis[14,15]. Our results revealed the downregulated expression of PD-L1 in CT26 cells by JQ1 treatment (Fig. 1D).

3.2. MΦ regulation by Pano/JQ1

TAM is a major constituent and accounts for about 20% of the composition in TIME[27]. The major subtypes of M1 and M2 play the opposite roles in tumorigenesis and development[28,29]. It has been demonstrated that HDACi suppressed the pro-tumor M2 phenotype of TAMs (TAM2) by repolarizing them toward an anti-tumor M1 phenotype (TAM1)[10,30]. The bone marrow-derived macrophages (BMDMs, MΦ) that differentiated into the M1 or M2 subtype were treated with the drugs. M2Φ was characterized by overexpressed CD206 while M1Φ was with overexpressed iNOS. Intratumoral accumulation of lactic acid can suppress anti-tumor immunity (both adaptive and innate immunity); for example, lactic acid may induce M2Φ polarization[22]. We found that Pano/JQ1 combination suppressed M2Φ polarization (Fig. 2A). Lactic acid production was reduced in M2Φ and the expression level of PKM2 was downregulated (Supporting Information Fig. S2). Phosphorylated STAT6 is an intrinsic key
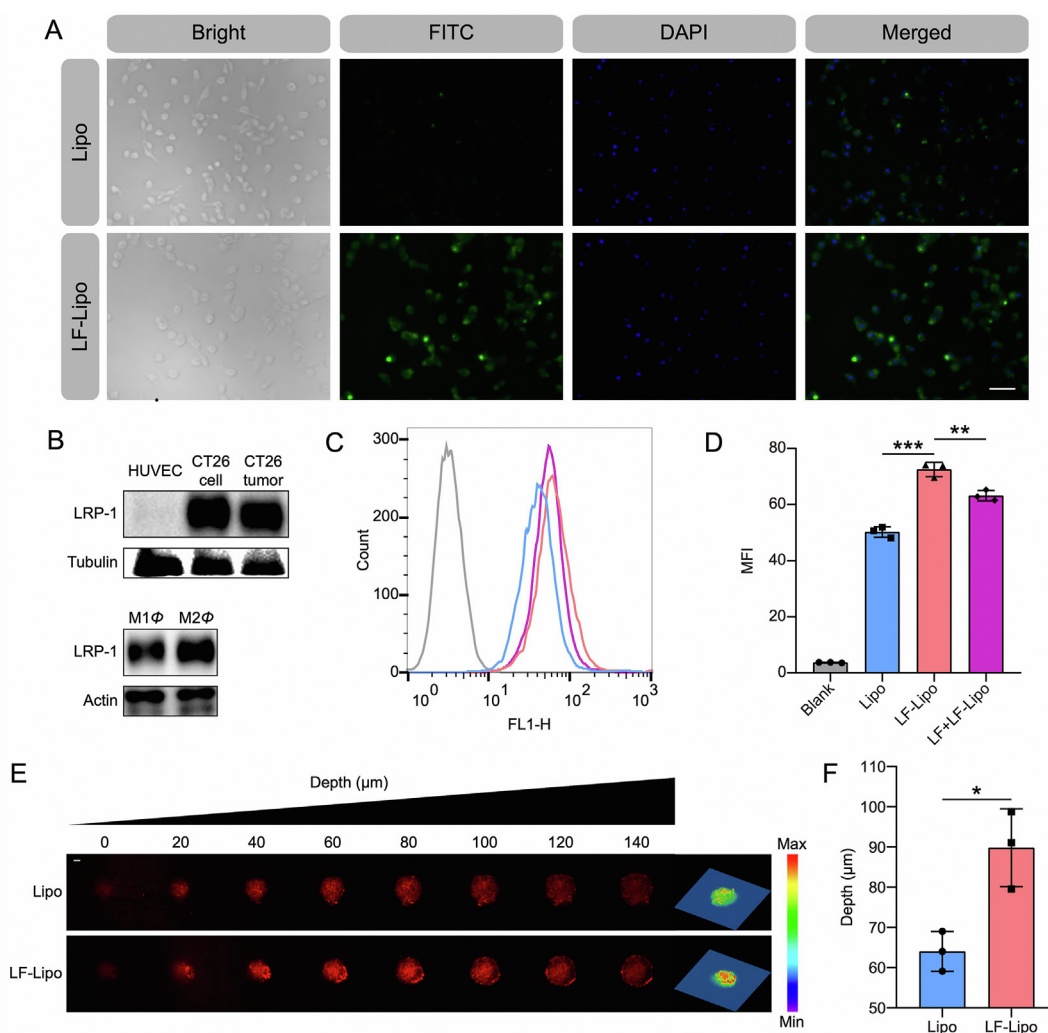

Figure 4 Cellular uptake and tumor spheroid penetration of the liposomes. (A) Fluorescence images of CT26 cells after treatment (scale bar = 50 μm). (B) LRP-1 expression of HUVEC, CT26 cell, CT26 tumor, M1Φ, and M2Φ. (C) Cellular uptake of liposomes with or without LF pre-treatment in CT26 cells. (D) Statistical analysis of cellular uptake efficiency in (C). (E) CLSM images of the *in vitro* penetration of LF-Lipo in the CT26 tumor spheroids (scale bar = 100 μm). (F) Quantitative analysis of the penetration depth in the CT26 tumor spheroids. Data are presented as mean ± SD ($n = 3$). *$P < 0.05$, **$P < 0.01$, ***$P < 0.001$.
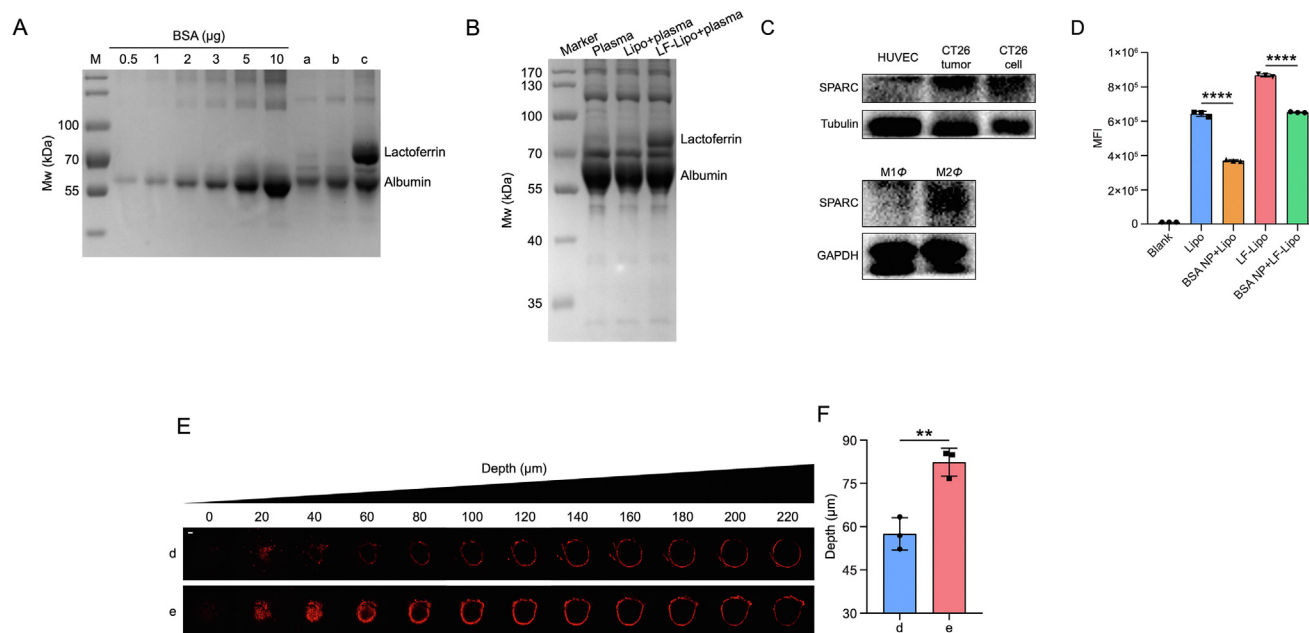
Figure 5 Albumin protein corona characterization of LF-Lipo. (A) The adsorption efficiency of albumin on Lipo and LF-Lipo. (a): cell culture medium; (b): Lipo/cell culture medium; (c): LF-Lipo/cell culture medium. (B) The adsorption of serum proteins on Lipo and LF-Lipo. (C) SPARC expression of HUVEC, CT26 cell, CT26 tumor, M1Φ, and M2Φ. (D) Statistical analysis of cellular uptake of liposomes with or without BSA NP pre-treatment in CT26 cells. (E) CLSM images of the *in vitro* penetration of the liposomes in CT26 tumor spheroids with serum-free cell culture medium pretreatment for 12 h (scale bar = 100 μm). (d): LF-Lipo/serum-free cell culture medium; (e): LF-Lipo/cell culture medium. (F) Quantitative analysis of the penetration depth in the CT26 tumor spheroids. Data are presented as mean ± SD (n = 3). **P < 0.01, ****P < 0.0001.

signaling that drives M2Φ polarization[31], and STAT6 was downstream of HDAC2[32]. Pano reduced STAT6 phosphorylation by inhibiting HDAC2 and thereby suppressed M2Φ polarization (Fig. 2A). The Pano/JQ1 combo also exhibited the effect of inducing M1 polarization (Fig. 2A and B). Also, the Pano/JQ1 group downregulated the BRD4 and PD-L1 expression in M2Φ, suggesting the potential effect on attenuating the immunosuppression in TME (Fig. 2A and C).

In the TME, various types of cells interact, and to mimic the TME, a transwell co-culture model of BMDMs/CT26 cells was used (Fig. 2D). The flow cytometry results demonstrated that the amounts of M2Φ and PD-L1$^+$ MΦ were significantly reduced in the Pano/JQ1 group compared to other treatments (Fig. 2E and F). The Pano/JQ1 treatment repolarized M2Φ even in the presence of CT26 cells, suggesting its effectiveness in TME. By using this experimental model, it indicated the potential treatment efficacy in TME.

3.3. Synthesis and characterization of dual-drug liposomes

The *in vitro* results revealed the synergistic effect of the combination therapy of Pano/JQ1. Therefore, a co-delivery liposomal system was developed for further enhancing the efficacy.

The LF-Lipo were prepared by a thin-film dispersion method and the surface-modified lactoferrin can specifically bind with the overexpressed LRP-1 in both the cancer cells and TAM. The non-modified Lipo was used as a control. The lactoferrin/liposome conjugation ratio was 0.16:1 (*w/w*), determined by SDS-PAGE (Fig. 3A). The particle size, morphological characterization, and zeta potential of LF-Lipo were shown in Fig. 3. LF-Lipo exhibited a spheroidal shape and a positive charge (Fig. 3B and C). Both liposomes remained stable at 37 °C in PBS

containing 10% fetal bovine serum (FBS) (Fig. 3D). The drug encapsulation efficiency of LF-Lipo was 76.4% for Pano and 88.0% for JQ1, and the drug-loading efficiency was 1.8% and 4.2%, respectively. Both Lipo and LF-Lipo had a sustained-release pattern (Fig. 3E).

3.4. Cellular uptake and in vitro penetration of LF-Lipo

After treatment with LF-Lipo, the CT26 cells were subjected to fluorescence microscopic observation and flow cytometric assay. The cellular uptake efficiency of LF-Lipo was higher than the non-modified Lipo (Fig. 4A). It was accounted for the overexpressed LRP-1 on the CT26 cells (Fig. 4B), which mediated intracellular delivery of LF-Lipo. The flow cytometry results further confirmed the superior LF-mediated delivery efficiency (Fig. 4C and D). More importantly, LRP-1 was also overexpressed in M2Φ (Fig. 4B). Similarly, the flow cytometry results also revealed that the cellular uptake of LF-Lipo in M2Φ was significantly higher than Lipo (Supporting Information Fig. S3A and B). The results indicated the promise of LF-mediated dual-targeting the cancer cells and TAMs *via* their overexpressed LRP-1 receptors.

The intratumoral penetration ability of LF-Lipo was evaluated in a cultured tumor cell spheroid model. LF-Lipo exhibited an enhanced penetration ability compared to Lipo, as demonstrated by CLSM Z-stack images (Fig. 4E and F). It indicated that LF/LRP-1-based effect could enhance the intratumor infiltration.

3.5. Albumin protein corona characterization of LF-Lipo

In the physiological environment, serum proteins were adsorbed on the nanoparticles and formed protein corona, which could change
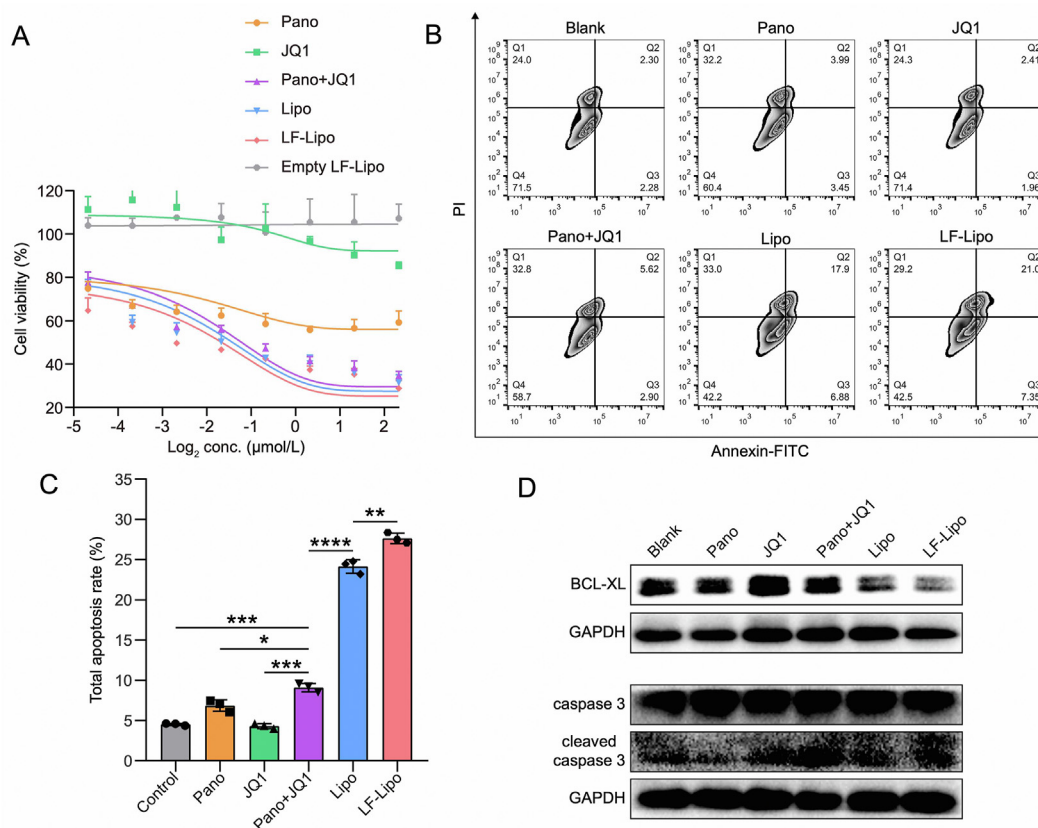
Figure 6 *In vitro* anti-tumor activity of LF-Lipo. (A) MTT assay of CT26 cells after treatment. (B) Apoptosis assay in CT26 cells *via* flow cytometry. (C) Statistical analysis of total apoptosis rate after treatment. (D) Expression of BCL-XL, caspase 3, and cleaved caspase 3 in CT26 cells after treatment. Data are presented as mean $\pm$ SD (n = 3). *P < 0.05, **P < 0.01, ***P < 0.001, ****P < 0.0001.

the biofate of the nanoparticles[33]. Serum albumin is the most abundant protein in the blood, accounting for 35−50 mg/mL. In specific, the adsorption of serum albumin on the liposome surface has been well acknowledged[34]. We found that the LF-Lipo adsorbed albumin that formed a protein corona on the surface and the albumin/liposome adsorption ratio was 0.1:1, determined by SDS-PAGE (Fig. 5A). Besides, the plasma/liposome co-incubation showed that the primary composition of the protein corona on the liposome was albumin (Fig. 5B).

The albumin-binding proteins (*e.g.*, SPARC) are highly expressed in tumors and responsible for the efficient uptake of albumin as a source of energy and amino acids for tumor growth. Therefore, albumin-based biomimetic drug delivery is a promising strategy for cancer therapy[35]. By taking advantage of the overexpressed SPARC in both CT26 cells and M2Φ (Fig. 5C), LF-Lipo exhibited a higher intracellular delivery efficiency than Lipo, but the intracellular uptake of both LF-Lipo and Lipo was reduced if the cells were pretreated with the empty BSA NP (Fig. 5D), due to the competitive binding. The results were consistent with our previous reports[36,37]. Different from free albumin, the liposome with albumin corona or the albumin nanoparticles could serve as multivalent binders with the membrane receptor albumin-binding proteins for facilitating delivery. It was reported that the clustering of the albumin-binding proteins on the cell surface can promote albumin transport[38,39].

The intratumoral penetration of LF-Lipo with albumin corona was evaluated in a cultured tumor cell spheroid model. Compared with LF-Lipo without albumin corona, LF-Lipo with albumin

corona exhibited an enhanced penetration ability, as demonstrated by CLSM Z-stack images (Fig. 5E and F). It indicated that the formation of albumin corona could enhance the intratumor infiltration of LF-Lipo.

3.6. *In vitro anti-tumor activity of LF-Lipo*

The IC$_{50}$ of Lipo is 0.37 µmol/L, while LF-Lipo is 0.27 µmol/L, indicating the higher anti-proliferation activity of LF-Lipo in the CT26 cancer cells (Fig. 6A). Of note, BMDMs showed a considerable tolerance to LF-Lipo compared to the CT26 cells (Supporting Information Fig. S3C).

Furthermore, LF-Lipo showed superior ability to induce apoptosis of CT26 cells (Fig. 6B and C), and the cleaved caspase 3 was upregulated while the anti-apoptosis protein BCL-XL was downregulated after treatment of LF-Lipo (Fig. 6D).

3.7. *Anti-angiogenesis by LF-Lipo*

HIF-1α/VEGF is a driving molecular signal axis for aerobic glycolysis and angiogenesis[40]. In the transwell co-culture system of CT26/BMDMs (Fig. 7A), Pano/JQ1 combination and LF-Lipo exhibited a potent ability to reverse M2 to M1 phenotype, evidenced by the downregulation of an M2-associated biomarker CD206 (Fig. 7B). It is known that M2 can promote tumor angiogenesis and aggravate hypoxia[41]. LF-Lipo significantly downregulated the expression of HIF-1α, VEGF, and PD-L1 in MΦ (Fig. 7B).
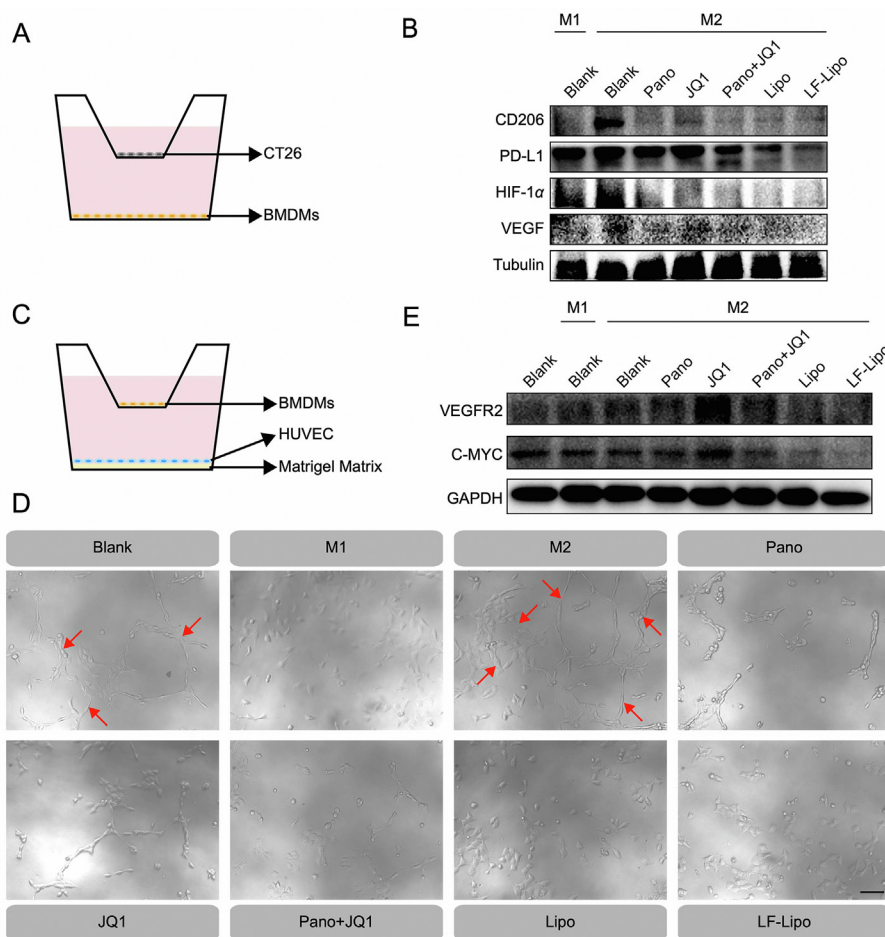
Figure 7 Anti-angiogenic effect of LF-Lipo. (A) Illustration of the co-culture system of CT26 cells and BMDMs. (B) Expression of CD206, PD-L1, HIF-1α, and VEGF in BMDMs co-cultured with CT26 cells. (C) Illustration of the co-culture system of HUVEC and BMDMs. (D) Endothelial cell tube formation (Red arrows) after drug treatment (scale bar = 100 μm). (E) Reduced VEGFR2 and C-MYC expression in HUVEC after treatment.

Accordingly, in the HUVEC/M2Φ co-culture system, the HUVEC tube formation was inhibited by LF-Lipo treatment (Fig. 7C and D). The anti-angiogenesis was attributed to the repolarization of M2Φ and the downregulation of HIF-1α and VEGF. The result was further confirmed by the downregulation of the crucial pro-angiogenic factors VEGFR2 and C-MYC in the HUVEC (Fig. 7E).

3.8. In vivo imaging and biodistribution of LF-Lipo

The *in vivo* imaging results showed that there was higher intratumoral accumulation in the LF-Lipo group than in the Lipo group (Fig. 8A). The *ex vivo* imaging further revealed the higher tumor-targeted efficiency of LF-Lipo (Fig. 8B and C).

To further demonstrate the LF-mediated targeting function, the co-localization of LF-Lipo and LRP-1 in the tumor cryosections was investigated by CLSM imaging. It showed that the DiR-labeled LF-Lipo largely overlapped with LRP-1 (Fig. 8D). Furthermore, the flow cytometry analysis also revealed that the positive rate of DiD$^+$/LRP-1$^+$ cells was higher in the LF-Lipo group than the Lipo group (Fig. 8E and F); both liposomes were labeled with DiD. It demonstrated that LF facilitated the uptake of LF-Lipo in the LRP-1$^+$ cells.

3.9. In vivo anti-tumor treatment of LF-Lipo in CT26 subcutaneous tumor model

The liposome-based delivery significantly enhanced the therapeutic efficacy; Lipo showed a tumor growth inhibition rate of 78.5% and LF-Lipo exhibited the highest efficacy of 95.3% (Fig. 9A−I). By contrast, the tumor growth inhibition rate of Pano was 50.7%, and that of the free combo drugs was 59.3%. Moreover, the H&E results indicated that LF-Lipo induced the highest necrosis rate in the tumors among all groups (Fig. 9J). The formation of central necrosis is associated with anti-angiogenesis by ceasing the blood flow[42].

A preliminary safety was evaluated by monitoring the body-weight change and the organ coefficient, as well as by performing the pathological examination. There were no obvious pathological changes, and these results indicated the biosafety of LF-Lipo treatment (Supporting Information Fig. S4).

3.10. Remodeling TME by LF-Lipo

The populations of the intratumor immune cells were determined. The amounts of immunosuppressive myeloid-derived suppressor

cells (MDSCs) and M2Φ were reduced after LF-Lipo treatment. By contrast, the anti-tumor natural killer (NK) cells and granzyme B$^+$ CD8$^+$ T cells were increased (Fig. 10A−D, Supporting Information Fig. S5). These results indicated that LF-Lipo treatment meliorated the immunosuppressive TME.

TME is characterized by excessive secretion of lactic acid and acidic conditions because of aerobic glycolysis[43]. In the LF-Lipo group, the intratumor level of lactic acid was significantly decreased compared to other groups (Fig. 10E). Moreover, an M2Φ marker CD206, immune checkpoint molecule PD-L1, metastatic marker TGF-β1, and the pro-angiogenesis factors VEGF and CD31 were downregulated while an M1Φ marker iNOS was upregulated by LF-Lipo treatment (Fig. 10F and G). These results demonstrated that the therapeutic mechanism of LF-Lipo was associated with remodeling TME by repolarizing MΦ and regulating tumor glycolysis and angiogenesis.

3.11. Anti-tumor treatment of LF-Lipo in CT26 peritoneal tumor model

Peritoneal metastasis occurs frequently in colorectal cancer patients[44], and there is a quarter incidence of peritoneal metastasis in the course of CRC[45]. Peritoneal metastasis is an indicator of poor prognosis and end-stage condition[46]. The peritoneal metastasis mouse model was developed by intraperitoneal injection of CT26-Luc cells, and the peritoneal tumor formation was confirmed by bioluminescence imaging (Supporting Information Fig. S6A and B).

The tumor-targeting ability of LF-Lipo was evaluated *via* *in vivo* and *ex vivo* imaging after intravenous injection of the DiR-labeled liposomes in the peritoneal tumor-bearing mice. LF-Lipo exhibited a higher accumulation at the peritoneum than Lipo. The *ex vivo* imaging also indicated a significantly higher accumulation in the LF-Lipo group than the Lipo group (Supporting Information Fig. S6C−F). It demonstrated that LF modification enhanced the targeting efficiency of delivery to the CT26 peritoneal tumor.

The therapeutic efficacy of LF-Lipo against peritoneal tumors was evaluated. LF-Lipo efficiently arrested tumor growth, with the highest inhibition rate (Fig. 11A and B). Besides, LF-Lipo exhibited a potent ability to remodel TIME and activate anti-tumor immunity. Specifically, M2Φ was reversed and MDSCs were decreased, as evidenced by the downregulation of CD206 and Gr-1 (Fig. 11C, Supporting Information Fig. S7). The LF-Lipo group also downregulated the intratumor level of lactic
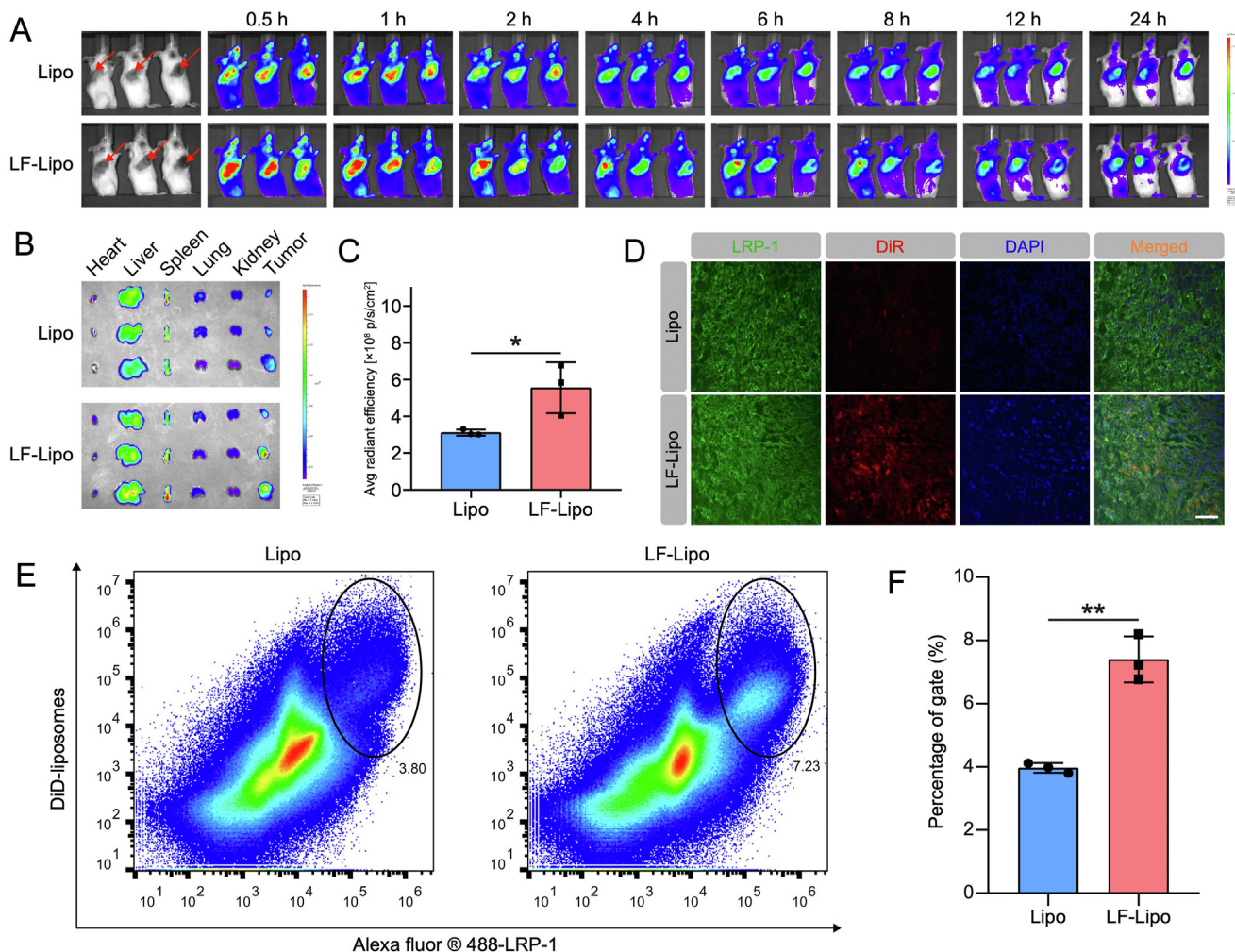

Figure 8 *In vivo* imaging and biodistribution of the liposomes in CT26 subcutaneous tumor model. (A) *In vivo* imaging from 0.5 h to 24 h. (B) *Ex vivo* imaging of major organs and tumors. (C) *Ex vivo* radiant efficiency of the tumors. (D) Immunofluorescence colocalization of the DiR dye-encapsulated liposomes and LRP-1 in the CT26 tumors (scale bar = 50 μm). (E) The population of DiD$^+$ LRP-1$^+$ cells in the tumor by flow cytometry. (F) Statistical analysis of DiD$^+$ LRP-1$^+$ cells. Data are presented as mean ± SD ($n = 3$). *$P < 0.05$, **$P < 0.01$.

acid significantly compared to other groups in the CT26 peritoneal tumor model (Fig. 11D). The flow cytometry results revealed that the amount of the TGF-β^+ MΦ was reduced and the granzyme B$^+$ CD8$^+$ T cells and IFN-γ^+ CD8$^+$ T cells were increased (Fig. 11E−G, Supporting Information Fig. S8). The ICH staining showed that PD-L1, CD31, TGF-β1, BRD4, and HDAC2 were reduced, too, after LF-Lipo treatment (Fig. 11H, Supporting Information Fig. S7). The inhibition of angiogenesis was demonstrated by the downregulation of an angiogenesis-related transcriptor HIF-1α, VEGF, and a tumor vessel marker CD31 (Fig. 11C and H).

3.12. Anti-tumor treatment of LF-Lipo + αPD-1 in CT26 subcutaneous tumor in situ recurrence model

The therapeutic efficacy of LF-Lipo + αPD-1 against the CT26 subcutaneous tumor recurrence model was evaluated. LF-Lipo + αPD-1 suppressed tumor growth effectively (Fig. 12A−I). Besides, LF-Lipo + αPD-1 also showed a potent ability to inhibit *in situ* tumor recurrence (Fig. 12J). These results indicated that LF-

Lipo + αPD-1 combination therapy could not only activate anti-tumor immune response but also maintain immune memory.

4. Discussion

Monotherapy hardly yields sustainable therapy outcomes because of drug tolerance and compensatory activation[47]. Combination therapy has become a regular regimen for complex diseases like cancer. Yet, the conventional combination is based on a practice of co-administration, instead of co-delivery. The co-administered drugs generally displayed distinct PK profiles, thus leading to a difficult prediction of synergistic effect. In 2017 the first dual-drug encapsulating liposomal product (Vyxeos®) was approved by the FDA for treating blood cancer. It represents a breakthrough in the field of co-delivery technology for combination therapy. Therefore, developing a co-delivery-based combination therapy strategy is a promising method for cancer therapy.

In this work, we proposed a strategy for epigenetic combination therapy for epigenetic modulation, through which the TIME was remodeled. It has been reported that the insensitivity of solid tumor
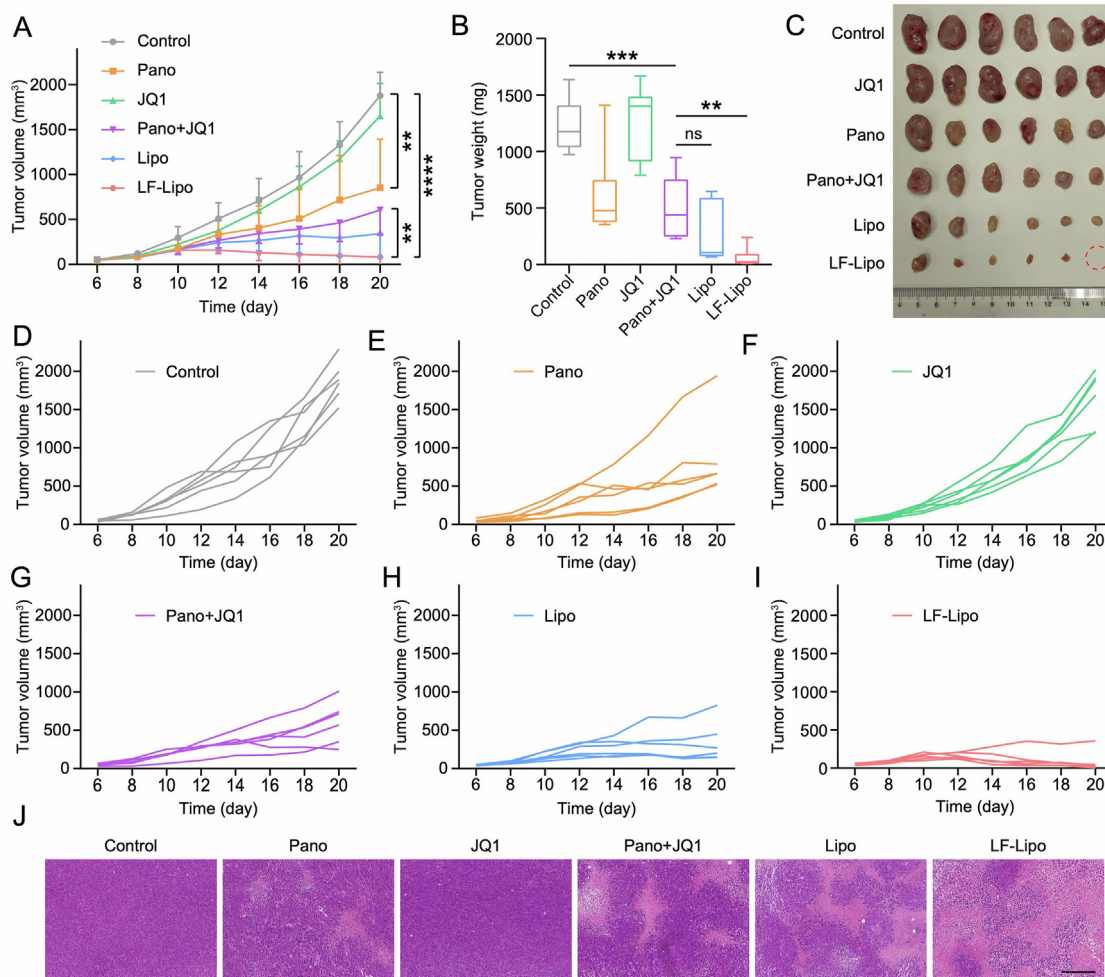

Figure 9 *In vivo* anti-tumor treatment in CT26 subcutaneous tumor model. (A) Tumor growth curve. (B) Tumor weight. (C) Tumor tissues. (D− I) Individual tumor growth curves of control, Pano, JQ1, Pano + JQ1, Lipo, and LF-Lipo groups. (J) Histological examination (purple color, indicating the normal tumor tissues; pink, indicating the necrotic tumor tissues) of CT26 subcutaneous tumors (scale bar = 200 μm). Data are presented as mean ± SD (*n* = 6). **P < 0.01, ***P < 0.001, ****P < 0.0001. ns, not significant.

cells to HDACi was associated with transcriptional activation of LIFR-JAK1-STAT3 signaling, and BRD4 inhibition augmented the efficacy of HDACi[48]. Other than acting on the intrinsic mechanism inside the cancer cells, this work revealed that TIME could also be a target for enhancing HDACi treatment efficacy. The effects of panobinostat on TAMs and TIME were reflected by the aspects as follows. Panobinostat downregulated PKM2, an essential metabolic enzyme of glycolysis in cancer cells, and thus reduced the production of lactic acid that is an immunosuppressor and contributes to unfavorable TIME. In addition, lactic acid can promote M2Φ polarization. Therefore, the reduced lactic acid was favorable for the suppression of M2Φ polarization. The ability to repolarize the TAM phenotype by panobinostat was related to the inhibition of STAT6 phosphorylation.

PD-L1 is an immune checkpoint molecule that is highly expressed on the tumor cells. It can bind to the PD-1 on the effector T cells or monocytes to suppress the anti-tumor immunity, thereby promoting tumor growth[49]. JQ1 is a small-molecular inhibitor of the BET family. It suppresses the transcriptional activity of PD-L1 and downregulates PD-L1 level by inhibiting the occupancy rate of BRD4 on the PD-L1 locus, thus activating the

specific anti-tumor immune response[15]. Besides, JQ1 can significantly reduce the proportion of tumor-infiltrating Treg cells[16], and inhibit the secretion of lactic acid of tumor cells[22]. Our work demonstrated that the combination therapy of the targeting liposomal Pano/JQ1 exhibited a synergistic effect on anti-tumor immunity and efficiently remodeled TIME as well as the tumor metabolism.

The interaction of cancer cells and immune cells facilitates the formation of the suppressive TIME by secreting cytokines and regulating metabolism. For example, tumor cells produce a large amount of lactic acid through aerobic glycolysis, making the microenvironment acidic[50], as well as inhibiting the DC maturation and the functions of effector T cells, impairing the adaptive immune responses[51]. Besides, lactic acid can promote the polarization of TAM to M2 and contribute to tumor immunosuppression by increasing the secretion of anti-inflammatory factors such as IL-10 and TGF-β[45]. Lactic acid can also induce VEGF expression by stabilizing the structure of HIF-1α, thus promoting tumor proliferation and migration[41]. Our results revealed that the liposomal Pano/JQ1 promoted immunity and vascular normalization.
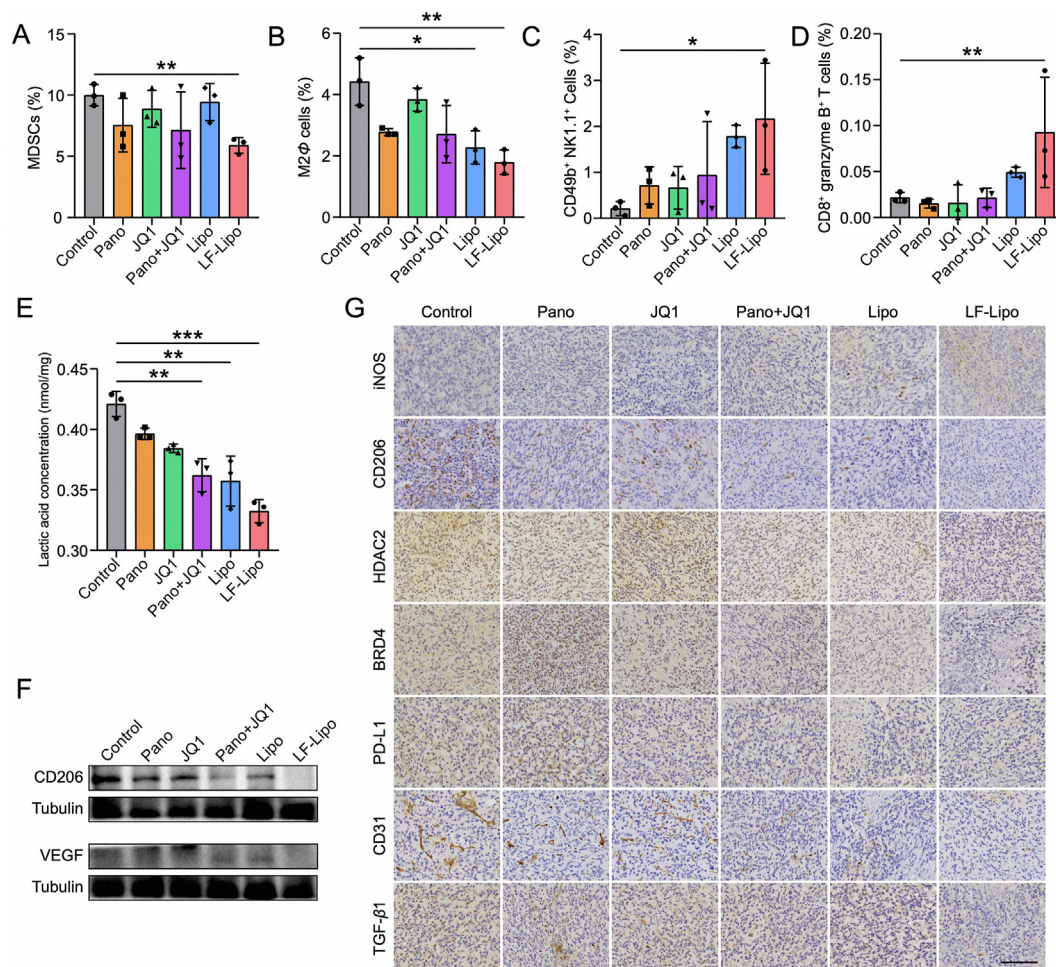

Figure 10 TME remodeling by the liposomes. The intratumoral percentage of MDSCs (A), M2Φ cells (B), CD49b$^+$ NK1.1$^+$ cells (C), CD8$^+$ granzyme B$^+$ T cells (D) after treatment. (E) The reduced lactic acid production in the tumors after treatment. (F) Expression of CD206 and VEGF in the tumors after treatment. (G) Immunohistochemical staining (brown color) of iNOS, CD206, HDAC2, BRD4, PD-L1, CD31, and TGF-β1 in CT26 subcutaneous tumors (scale bar = 100 μm). Data are presented as mean ± SD (n = 3). *P < 0.05, **P < 0.01, ***P < 0.001.

Another interesting finding of this work was the demonstration of the *in situ* formation of albumin corona further promoting the targeting delivery efficiency. Protein corona formation on the surface of liposomes has attracted great attention for the effect on modulating biofate of the liposomes[34]. The albumin-mediated biomimetic delivery strategy has been widely applied *via* a mechanism of targeting the overexpressed albumin-binding proteins on the tumor cells and TAMs[36,37,52]. It was reported that the induction of clusters of the receptors (*e.g.*, albumin-binding proteins) on the cells facilitated the albumin transport[53]. Therefore, the albumin-decorated nanoparticles could act as a recruiter for clustering the albumin-binding receptors because the nanoparticles can simultaneously bind with multiple receptors and thus induce clustering. Our work revealed that the LF-modified liposomes actually processed the dual-targeting function. The *in situ*-

formation of albumin corona in cancer drug delivery is worthy of further investigation.

5. Conclusions

In this work, we developed the chemo-free binary-drug liposomes with *in situ*-formed albumin corona for remodeling the tumor microenvironment *via* epigenetic-based therapy. LRP-1 and SPARC overexpressed on the colorectal tumor cells and TAMs could serve as the co-delivery targets for LF-Lipo. Moreover, by activating the anti-tumor immunity responses, inhibiting lactic acid secretion, and limiting angiogenesis, LF-Lipo suppressed tumor growth and metastasis. This liposome-based synergistic therapy provides a useful avenue for overcoming the "cold" tumor and offers a promising combination of epigenetic drugs for triggering immune responses.
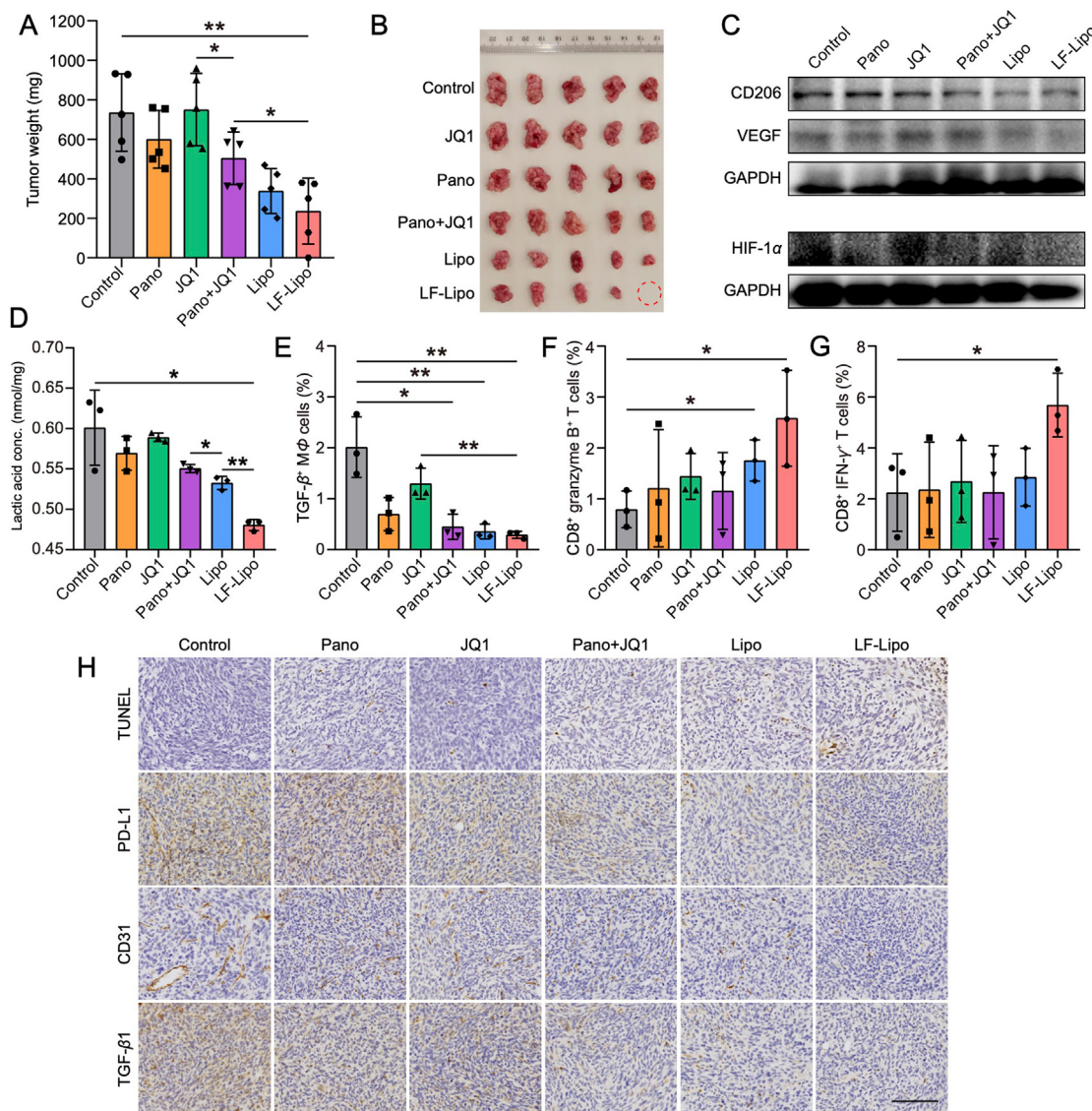

Figure 11 *In vivo* anti-tumor treatment of the liposomes in CT26 peritoneal tumor model. (A) Tumor weight at the experimental endpoint. (B) Tumor images. (C) Expression of HIF-1α, VEGF, and CD206 in CT26 peritoneal tumors after treatment. (D) The reduced lactic acid production in CT26 peritoneal tumors after treatment. The percentage of TGF-β^+ MΦ (E), CD8$^+$ granzyme B$^+$ T cells (F), CD8$^+$ IFN-γ^+ T cells (G) in CT26 peritoneal tumors after treatment. (H) TUNEL assay of apoptosis and immunohistochemical staining (brown color) of PD-L1, CD31, and TGF-β1 in CT26 peritoneal tumors after treatment (scale bar = 100 μm). Data are presented as mean ± SD (A, B, $n = 5$; D, E, F, G, $n = 3$). *$P < 0.05$, **$P < 0.01$.
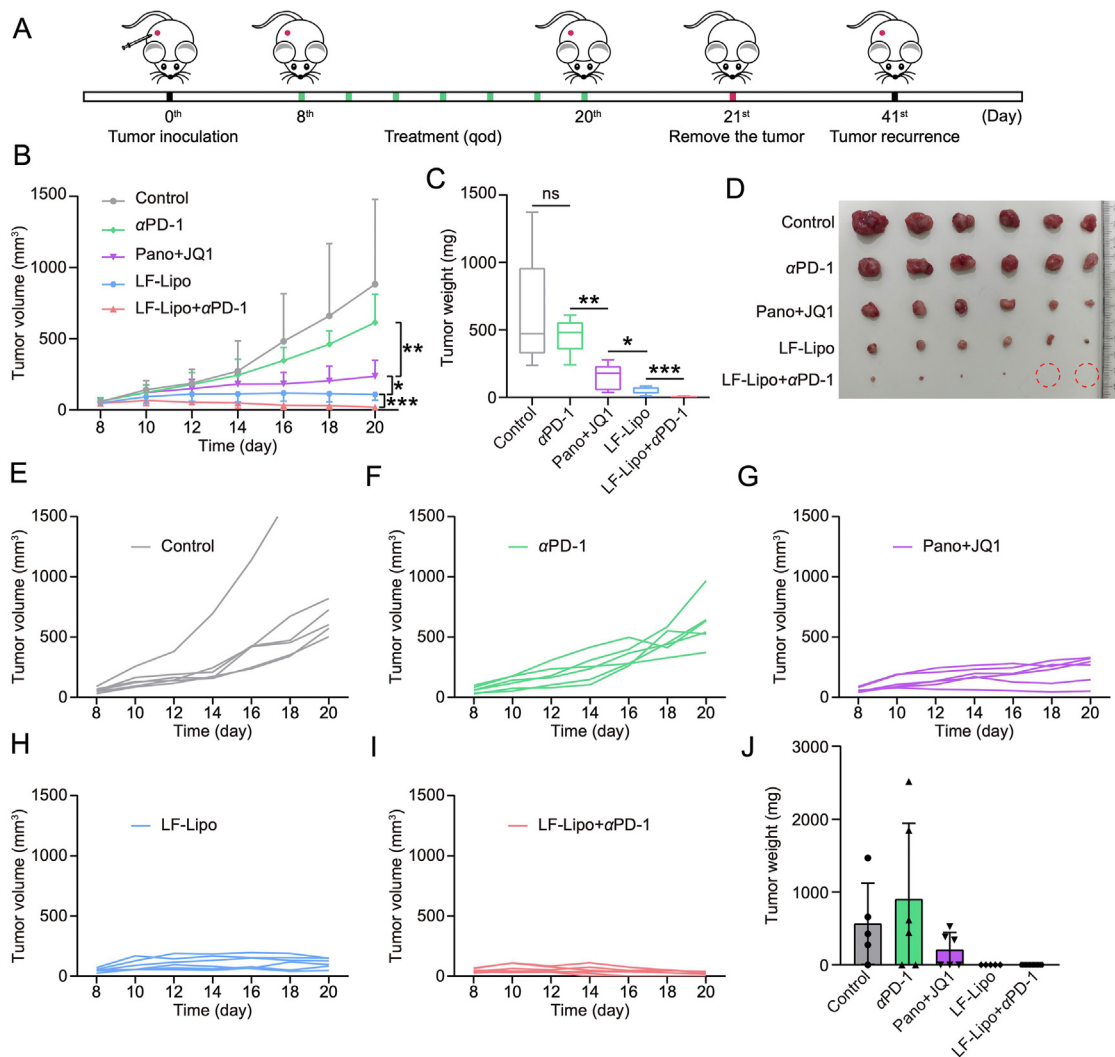
Figure 12 *In vivo* anti-tumor treatment of LF-Lipo + αPD-1 in CT26 subcutaneous tumor *in situ* recurrence model. (A) Therapeutic schedule. (B) Tumor growth curve. (C) Tumor weight of the primary tumor. (D) Tumor tissues. (E–I) Individual tumor growth curves of control, αPD-1, Pano + JQ1, LF-Lipo, and LF-Lipo + αPD-1 groups. (J) Tumor weight of the recurrent tumor after surgical removal of the primary tumors. Data are presented as mean ± SD ($n = 6$). *$P < 0.05$, **$P < 0.01$, ***$P < 0.001$. ns, not significant.

Acknowledgments

Author contributions

Yongzhuo Huang, Yang He, and Yuefei Fang designed the research and performed data analysis. Yang He, Yuefei Fang, and Meng Zhang carried out the experiments. Yuge Zhao, Bin Tu, and Mingjie Shi participated part of the experiments. Yang He wrote the manuscript. Yongzhuo Huang revised the manuscript. All of the authors have read and approved the final manuscript.

Conflicts of interest

The authors have no conflicts of interest to declare.

Appendix A.   Supporting information

Supporting data to this article can be found online at https://doi.org/10.1016/j.apsb.2021.09.022.

References

1. Ma YS, Wu ZJ, Zhang HW, Cai B, Huang T, Long HD, et al. Dual regulatory mechanisms of expression and mutation involving metabolism-related genes FDFT1 and UQCR5 during CLM. *Mol Ther Oncolytics* 2019;**14**:172−8.

2. Jackstadt R, Van Hooff SR, Leach JD, Cortes-Lavaud X, Lohuis JO, Ridgway RA, et al. Epithelial NOTCH signaling rewires the tumor microenvironment of colorectal cancer to drive poor-prognosis subtypes and metastasis. *Cancer Cell* 2019;**36**:319−36.

3. Dienstmann R, Vermeulen L, Guinney J, Kopetz S, Tejpar S, Tabernero J. Consensus molecular subtypes and the evolution of precision medicine in colorectal cancer. *Nat Rev Cancer* 2017;**17**:79−92.

4. Ganesh K, Stadler ZK, Cercek A, Mendelsohn RB, Shia J, Segal NH, et al. Immunotherapy in colorectal cancer: rationale, challenges and potential. *Nat Rev Gastroenterol Hepatol* 2019;**16**:361−75.

5. Mccaw TR, Randall TD, Forero A, Buchsbaum DJ. Modulation of antitumor immunity with histone deacetylase inhibitors. *Immunotherapy* 2017;**9**:1359−72.

6. Eckschlager T, Plch J, Stiborova M, Hrabeta J. Histone deacetylase inhibitors as anticancer drugs. *Int J Mol Sci* 2017;**18**:1414.

7. Zhao LM, Zhang JH. Histone deacetylase inhibitors in tumor immunotherapy. *Curr Med Chem* 2019;**26**:2990−3008.

8. Lindemann RK, Gabrielli B, Johnstone RW. Histone-deacetylase inhibitors for the treatment of cancer. *Cell Cycle* 2004;**3**:777−86.

9. Tu B, Zhang M, Liu T, Huang Y. Nanotechnology-based histone deacetylase inhibitors for cancer therapy. *Front Cell Dev Biol* 2020;**8**:400.

10. Peng H, Chen B, Huang W, Tang Y, Jiang Y, Zhang W, et al. Reprogramming tumor-associated macrophages to reverse EGFR(T790M) resistance by dual-targeting codelivery of Gefitinib/Vorinostat. *Nano Lett* 2017;**17**:7684−90.

11. Jiang H, Zhang S, Song T, Guan X, Zhang R, Chen X. Trichostatin a protects dendritic cells against oxygen-glucose deprivation *via* the SRSF3/PKM2/glycolytic pathway. *Front Pharmacol* 2018;**9**:612.

12. Miranda-Gonçalves V, Lameirinhas A, Henrique R, Jerónimo C. Metabolism and epigenetic interplay in cancer: regulation and putative therapeutic targets. *Front Genet* 2018;**9**:427.

13. Woods DM, Woan K, Cheng F, Wang H, Perez-Villarroel P, Lee C, et al. The antimelanoma activity of the histone deacetylase inhibitor panobinostat (LBH589) is mediated by direct tumor cytotoxicity and increased tumor immunogenicity. *Melanoma Res* 2013;**23**:341−8.

14. Zhu H, Bengsch F, Svoronos N, Rutkowski MR, Bitler BG, Allegrezza MJ, et al. BET bromodomain inhibition promotes antitumor immunity by suppressing PD-L1 expression. *Cell Rep* 2016;**16**:2829−37.

15. Hogg SJ, Vervoort SJ, Deswal S, Ott CJ, Li J, Cluse LA, et al. BET-bromodomain inhibitors engage the host immune system and regulate expression of the immune checkpoint ligand PD-L1. *Cell Rep* 2017;**18**:2162−74.

16. Adeegbe DO, Liu S, Hattersley MM, Bowden M, Zhou CW, Li S, et al. BET bromodomain inhibition cooperates with PD-1 blockade to facilitate antitumor response in Kras-mutant non−small cell lung cancer. *Cancer Immunol Res* 2018;**6**:1234−45.

17. He ZD, Zhang M, Wang YH, He Y, Wang HR, Chen BF, et al. Anti-PD-L1 mediating tumor-targeted codelivery of liposomal irinotecan/JQ1 for chemo-immunotherapy. *Acta Pharmacol Sin* 2021;**42**:1516−23.

18. Topper MJ, Vaz M, Marrone KA, Brahmer JR, Baylin SB. The emerging role of epigenetic therapeutics in immuno-oncology. *Nat Rev Clin Oncol* 2020;**17**:75−90.

19. Xu X, Lv J, Guo F, Li J, Jia Y, Jiang D, et al. Gut microbiome influences the efficacy of PD-1 antibody immunotherapy on MSS-type colorectal cancer *via* metabolic pathway. *Front Microbiol* 2020;**11**:814.

20. Tauriello DVF, Palomo-Ponce S, Stork D, Berenguer-Llergo A, Badia-Ramentol J, Iglesias M, et al. TGFbeta drives immune evasion in genetically reconstituted colon cancer metastasis. *Nature* 2018;**554**:538−43.

21. Etman SM, Abdallah OY, Mehanna RA, Elnaggar YSR. Lactoferrin/hyaluronic acid double-coated lignosulfonate nanoparticles of quinacrine as a controlled release biodegradable nanomedicine targeting pancreatic cancer. *Int J Pharm* 2020;**578**:119097.

22. Wang H, Tang Y, Fang Y, Zhang M, Wang H, He Z, et al. Reprogramming tumor immune microenvironment (TIME) and metabolism *via* biomimetic targeting codelivery of Shikonin/JQ1. *Nano Lett* 2019;**19**:2935−44.

23. Zhu Y, Yu X, Thamphiwatana SD, Zheng Y, Pang Z. Nanomedicines modulating tumor immunosuppressive cells to enhance cancer immunotherapy. *Acta Pharm Sin B* 2020;**10**:2054−74.

24. Nguyen VH, Lee BJ. Protein corona: a new approach for nanomedicine design. *Int J Nanomedicine* 2017;**12**:3137−51.

25. Miranda-Goncalves V, Lameirinhas A, Henrique R, Jeronimo C. Metabolism and epigenetic interplay in cancer: regulation and putative therapeutic targets. *Front Genet* 2018;**9**:427.

26. Nguyen TTT, Zhang Y, Shang E, Shu C, Torrini C, Zhao J, et al. HDAC inhibitors elicit metabolic reprogramming by targeting super-enhancers in glioblastoma models. *J Clin Invest* 2020;**130**:3699−716.

27. Faget J, Groeneveld S, Boivin G, Sankar M, Zangger N, Garcia M, et al. Neutrophils and snail orchestrate the establishment of a pro-tumor microenvironment in lung cancer. *Cell Rep* 2017;**21**:3190−204.

28. Jin H, He Y, Zhao P, Hu Y, Tao J, Chen J, et al. Targeting lipid metabolism to overcome EMT-associated drug resistance *via* integrin beta3/FAK pathway and tumor-associated macrophage repolarization using legumain-activatable delivery. *Theranostics* 2019;**9**:265−78.

29. Yin W, Yu X, Kang X, Zhao Y, Zhao P, Jin H, et al. Remodeling tumor-associated macrophages and neovascularization overcomes EGFR(T790M)-associated drug resistance by PD-L1 nanobody-mediated codelivery. *Small* 2018;**14**:e1802372.

30. Guerriero JL, Sotayo A, Ponichtera HE, Castrillon JA, Pourzia AL, Schad S, et al. Class IIa HDAC inhibition reduces breast tumours and metastases through anti-tumour macrophages. *Nature* 2017;**543**:428−32.

31. Chen W, Wang J, Jia L, Liu J, Tian Y. Attenuation of the programmed cell death-1 pathway increases the M1 polarization of macrophages induced by zymosan. *Cell Death Dis* 2016;**7**:e2115.

32. Buglio D, Georgakis GV, Hanabuchi S, Arima K, Khaskhely NM, Liu YJ, et al. Vorinostat inhibits STAT6-mediated TH2 cytokine and TARC production and induces cell death in Hodgkin lymphoma cell lines. *Blood* 2008;**112**:1424−33.

33. Abstiens K, Maslanka Figueroa S, Gregoritza M, Goepferich AM. Interaction of functionalized nanoparticles with serum proteins and its impact on colloidal stability and cargo leaching. *Soft Matter* 2019;**15**:709−20.

34. Caracciolo G. Liposome-protein corona in a physiological environment: challenges and opportunities for targeted delivery of nanomedicines. *Nanomedicine* 2015;**11**:543−57.

35. Zhao P, Wang Y, Wu A, Rao Y, Huang Y. Roles of albumin-binding proteins in cancer progression and biomimetic targeted drug delivery. *ChemBioChem* 2018;**19**:1796−805.

36. Zhao PF, Yin WM, Wu AH, Tang YS, Wang JY, Pan ZZ, et al. Dual-targeting to cancer cells and M2 macrophages *via* biomimetic delivery of mannosylated albumin nanoparticles for drug-resistant cancer therapy. *Adv Funct Mater* 2017;**27**:1700403.

37. Zhao P, Wang Y, Kang X, Wu A, Yin W, Tang Y, et al. Dual-targeting biomimetic delivery for anti-glioma activity *via* remodeling the tumor microenvironment and directing macrophage-mediated immunotherapy. *Chem Sci* 2018;**9**:2674−89.

38. Vogel SM, Minshall RD, P M, Tiruppathi C, Malik AB. Albumin uptake and transcytosis in endothelial cells *in vivo* induced by albumin-binding protein. *Am J Physiol Lung Cell Mol Physiol* 2001;**281**:1512−22.

39. Zhao P, Yin W, Wu A, Tang Y, Wang J, Pan Z, et al. Dual-targeting to cancer cells and M2 macrophages *via* biomimetic delivery of mannosylated albumin nanoparticles for drug-resistant cancer therapy. *Adv Funct Mater* 2017;**27**:1700403.

40. Noy R, Pollard JW. Tumor-associated macrophages: from mechanisms to therapy. *Immunity* 2014;**41**:49−61.

41. Colegio OR. Lactic acid polarizes macrophages to a tumor-promoting state. *Oncoimmunology* 2016;**5**:e1014774.

42. Yoshida S, Kawai H, Eguchi T, Sukegawa S, Oo MW, Anqi C, et al. Tumor angiogenic inhibition triggered necrosis (TAITN) in oral cancer. *Cells* 2019;**8**:761.

43. Hanahan D, Weinberg RA. Hallmarks of cancer: the next generation. *Cell* 2011;**144**:646−74.

44. Lee Ju-Hee, Ahn Byung Kyu, Baik Seung Sam, Lee Kang Hong. Comprehensive analysis of somatic mutations in colorectal cancer with peritoneal metastasis. *In Vivo* 2019;**33**:447−52.

45. Chen B, Gao A, Tu B, Wang Y, Yu X, Wang Y, et al. Metabolic modulation *via* mTOR pathway and anti-angiogenesis remodels tumor microenvironment using PD-L1-targeting codelivery. *Biomaterials* 2020;**255**:120187.

46. Lu Z, Wang J, Wientjes MG, Au JL. Intraperitoneal therapy for peritoneal cancer. *Future Oncol* 2010;**6**:1625−41.

47. Mendez-Lucas A, Lin W, Driscoll PC, Legrave N, Novellasdemunt L, Xie C, et al. Identifying strategies to target the metabolic flexibility of tumours. *Nat Metab* 2020;**2**:335−50.

48. Zeng H, Qu J, Jin N, Xu J, Lin C, Chen Y, et al. Feedback activation of leukemia inhibitory factor receptor limits response to histone deacetylase inhibitors in breast cancer. *Cancer Cell* 2016;**30**:459−73.

49. Balar AV, Weber JS. PD-1 and PD-L1 antibodies in cancer: current status and future directions. *Cancer Immunol Immunother* 2017;**66**:551−64.

50. Shamsi M, Saghafian M, Dejam M, Sanati-Nezhad A. Mathematical modeling of the function of Warburg effect in tumor microenvironment. *Sci Rep* 2018;**8**:8903.

51. Pearce EL, Poffenberger MC, Chang CH, Jones RG. Fueling immunity: insights into metabolism and lymphocyte function. *Science* 2013;**342**:1242454.

52. Zhao P, Zhang J, Wu A, Zhang M, Zhao Y, Tang Y, et al. Biomimetic codelivery overcomes osimertinib-resistant NSCLC and brain metastasis *via* macrophage-mediated innate immunity. *J Control Release* 2021;**329**:1249−61.

53. Vogel SM, Minshall RD, Pilipovic M, Tiruppathi C, Malik AB. Albumin uptake and transcytosis in endothelial cells *in vivo* induced by albumin-binding protein. *Am J Physiol Lung Cell Mol Physiol* 2001;**281**:L1512−22.